

Asteroids in the Inner Solar System II – Observable Properties

N.W. Evans¹ and S.A. Tabachnik^{1,2}

¹ *Theoretical Physics, 1 Keble Rd, Oxford, OX1 3NP*

² *Princeton University Observatory, Princeton, NJ 08544-1001, USA*

ABSTRACT

This paper presents synthetic observations of long-lived, coorbiting asteroids of Mercury, Venus, the Earth and Mars. Our sample is constructed by taking the limiting semimajor axes, differential longitudes and inclinations for long-lived stability provided by simulations. The intervals are randomly populated with values to create initial conditions. These orbits are re-simulated to check that they are stable and then re-sampled every 2.5 years for 1 million years. The Mercurian sample contains only horseshoe orbits, the Martian sample only tadpoles.

For both Venus and the Earth, the greatest concentration of objects on the sky occurs close to the classical Lagrange points at heliocentric ecliptic longitudes of 60° and 300° . The distributions are broad especially if horseshoes are present in the sample. The full-width half maximum (FWHM) in heliocentric longitude for Venus is 325° and for the Earth is 328° . The mean and most common velocity of these coorbiting satellites coincides with the mean motion of the parent planet, but again the spread is wide with a FWHM for Venus of $27.8'' \text{ hr}^{-1}$ and for the Earth of $21.0'' \text{ hr}^{-1}$. For Mars, the greatest concentration on the sky occurs at heliocentric ecliptic latitudes of $\pm 12^\circ$. The peak of the velocity distribution occurs at $65'' \text{ hr}^{-1}$, significantly less than the Martian mean motion, while its FWHM is $32.3'' \text{ hr}^{-1}$. The case of Mercury is the hardest of all, as the greatest concentrations occur at heliocentric longitudes of 16.0° and 348.5° and so are different from the classical values. The fluctuating eccentricity of Mercury means that these objects can have velocities exceeding $1000'' \text{ hr}^{-1}$, although the most common velocity is $459'' \text{ hr}^{-1}$, which is much less than the Mercurian mean motion.

A variety of search strategies are discussed, including wide-field CCD imaging, space satellites such as *The Global Astrometry Interferometer for Astrophysics* (GAIA), ground-based surveys like *The Sloan Digital Sky Survey* (SDSS), as well as infrared cameras and space-borne coronagraphs.

Key words: Solar System: general – minor planets, asteroids – planets and satellites: individual: Mercury, Venus, the Earth, Mars

1 INTRODUCTION

Even though the inner Solar System is seemingly very empty of asteroids, the suspicion is that this may be caused by the observational awkwardness of locating fast moving objects at small solar elongations. Observations of the Lagrange points of Mercury, Venus and the Earth can only be obtained in the mornings or evenings, and are hindered by high airmasses (e.g., Whiteley & Tholen 1998).

There have been sporadic searches for Trojans of the Earth and Mars before. With the exception of the two Martian Trojans, 5261 Eureka (e.g., Holt & Levy 1990; Mikkola et al. 1994) and 1998 VF31 (e.g., *Minor Planet Circular* 33085; Tabachnik & Evans 1999), these searches have been

without success. In particular, Weissman & Wetherill (1974) and Dunbar & Helin (1983) used photographic plates, while Whiteley & Tholen (1998) used CCD cameras, to look unavailingly for terrestrial Trojans. We are unaware of any observational surveys of the Lagrange points of Venus, although some tentative strategies for Mercurian Trojans have been suggested (e.g., Campins et al. 1996).

Recent technological advances have re-invigorated interest in this problem. There are at least two promising lines of attack. First, very large format CCD arrays are now being built. Wide-field CCD imaging has already transformed our knowledge of the outer Solar System with the discoveries of over two hundred faint trans-

Planet	<i>N</i>	<i>i</i>	λ	a/a_p
Mercury	583	$0^\circ - 10^\circ$	$325^\circ - 35^\circ$	$0.9988 - 1.0012$
Venus	2000	$0^\circ - 16^\circ$	$15^\circ - 345^\circ$	$0.996 - 1.004$
Earth	2000	$0^\circ - 40^\circ$	$10^\circ - 350^\circ$	$0.994 - 1.006$
Mars	500	$8^\circ - 40^\circ$	$30^\circ - 130^\circ$	1.000
Mars	500	$10^\circ - 40^\circ$	$230^\circ - 330^\circ$	1.000

Table 1. This shows the number of test particles for each planet. The initial conditions are drawn uniformly from the ranges in inclination i , differential longitude λ and semimajor axis a shown. These test particles are integrated for 1 million years to provide the survivors recorded in Table 2.

Neptunian or Kuiper-Edgeworth belt objects (e.g., Luu & Jewitt 1998; Jewitt & Luu 1999). The same strategies may well bear fruit in the inner Solar System, with the Lagrange points of the terrestrial planets obvious target locations. A second way of finding asteroids in the inner Solar System is by exploiting the large databases to be provided by satellites like *The Global Astrometry Interferometer for Astrophysics* (GAIA, see “<http://astro.estec.esa.nl/SA-general/Projects/GAIA/gaia.html>”). Ground-based surveys like *The Sloan Digital Sky Survey* (SDSS, see “<http://www.sdss.org/>”) will also be useful for objects exterior to the Earth’s orbit.

Motivated by these observational opportunities, this paper presents the observable properties of numerically long-lived clouds of asteroids orbiting about the Lagrange points of the terrestrial planets. Our clouds are generated from our earlier numerical integrations of test particles for timescales up to 100 million years (Tabachnik & Evans 2000, henceforth Paper I). These are the longest currently available integrations, although of course they span a small fraction of the estimated 5 Gyr age of the Solar System. The survivors from our earlier integrations are re-simulated and re-sampled to provide the distributions of observables. These include the contours of probability density on the sky, as well as the distributions of proper motions and the brightnesses.

The paper discusses our strategy for constructing the observable properties of clouds of coorbiting asteroids in Section 2. Venus, the Earth and Mars are examined in Sections 3, 4 and 5. The case of Mercury, the hardest of all, is postponed to Section 6. For each planet, we discuss both the synthetic observations and the optimum search strategy.

2 SIMULATIONS AND SYNTHETIC OBSERVATIONS

With the results of Paper I in hand, it is straightforward to build initial populations of stable test particles coorbiting with each of the terrestrial planets. For Venus, the Earth and Mars, Figures 6, 10, 11, 13 and 16 of Paper I are used to provide limiting values for the semimajor axes, differential longitudes and inclinations, as listed in Table 1. The intervals are replenished uniformly with random values in order to create sets of 2000 initial conditions in the case of Venus and the Earth, 1000 in the case of Mars. In all cases,

Planet	Survivors (Sample I)	Trojans at L_4 (Sample II)	Trojans at L_5 (Sample II)
Mercury	321	-	-
Venus	1691	359	346
Earth	982	227	202
Mars	909	487	422

Table 2. This shows the number of survivors around the Lagrange points of each planet remaining after the 1 Myr integration. Sample I comprises all the stable orbits, whether horseshoes or tadpoles. Sample II is just the tadpole orbits.

initial eccentricities, longitudes of ascending node and mean anomalies coincide with the parent planet. This collection of test particles is integrated for 1 Myr and any test particles that enter the sphere of influence of a planet or become hyperbolic are removed. Therefore, the number of objects in the final samples vary from planet to planet and is recorded in Table 2. For Venus and the Earth, results are presented for two samples. The first (henceforth Sample I) comprises stable tadpole and horseshoe orbits, the second (Sample II) only tadpole or truly Trojan orbits. For Mars, the entire sample is tadpole orbits, as no horseshoes survived the integrations of Paper I. (The case of Mercury is different and is discussed in Section 6).

Once the population of long-lived test particles has been generated, they are integrated again for 1 Myr. The positions and velocities are then sampled every 2.5 yr in various reference frames and several coordinate systems to generate our synthetic observations. In particular, it is useful to present results in geocentric ecliptic longitude and latitude (ℓ_g, β_g) in which the vantage point is the Earth and the Sun is in the direction $(\ell_g = 0^\circ, \beta_g = 0^\circ)$. The location of the L_4 and L_5 points in geocentric ecliptic coordinates differs from planet to planet. Sometimes, we also use heliocentric ecliptic latitude and longitude coordinates (ℓ_h, β_h) , in which the Sun is at the origin and the planet under scrutiny lies in the direction $(\ell_h = 0^\circ, \beta_h = 0^\circ)$. Now the leading L_4 cloud is always roughly centered on $(\ell_h = 60^\circ, \beta_h = 0^\circ)$ and the trailing L_5 cloud at $(\ell_h = 300^\circ, \beta_h = 0^\circ)$. The angular velocities in the plane of, and perpendicular to, the ecliptic are also sampled. It is useful to know the distribution of velocities as this determines the observing strategy. Finally, it is also helpful to know where the brightest asteroids lie. This is of course controlled by the position, size and albedo of the asteroid. The latter two quantities are unknown, but the effects of the change of brightness with position can be investigated by monitoring the magnitude adjustment Δm_V (c.f., Wiegert, Innanen & Mikkola 2000). This is the difference between the apparent magnitude m_V and the absolute magnitude H_V for each test particle. In other words,

$$\Delta m_V = m_V(\alpha, r, \Delta) - H_V, \quad (1)$$

where α is the solar phase angle (the angle subtended by the Sun-asteroid-Earth system), while r and Δ are the heliocentric and geocentric distances of the asteroid. Using the IAU two-parameter magnitude system (Bowell et al. 1989), the magnitude adjustment is

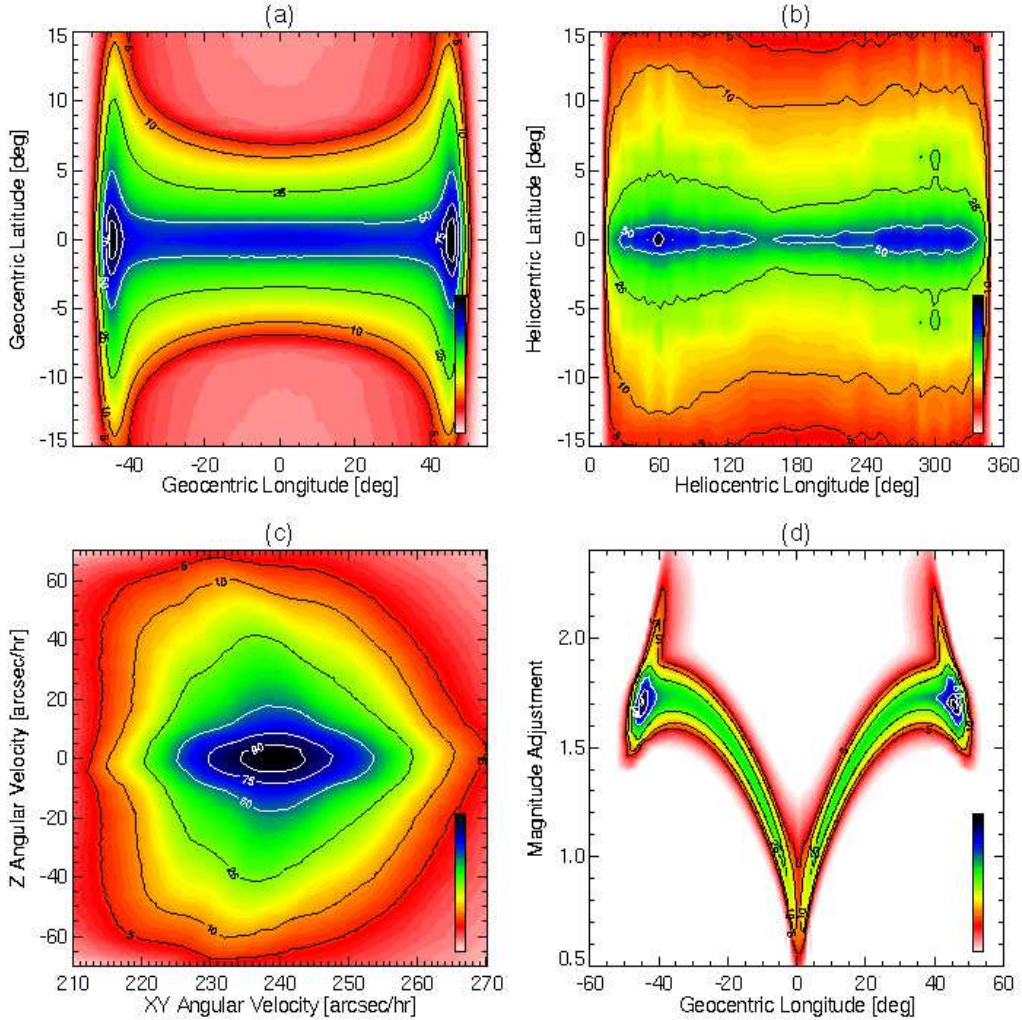


Figure 1. This shows the observable properties of Sample I of long-lived horseshoe and tadpole orbits around the Venusian Lagrange points. The panels illustrate the probability density in the planes of (a) geocentric ecliptic latitude and longitude, (b) heliocentric ecliptic latitude and longitude, (c) angular velocity in the ecliptic ($X - Y$) versus angular velocity perpendicular (Z) to the ecliptic, and (d) magnitude adjustment versus geocentric longitude. In this and subsequent figures, the colour scale ranges from deep blue (90% contour) through green (50%) to red (10%).

$$\Delta m_V = -2.5 \log[(1 - G)\Phi_1(\alpha) + \Phi_2(\alpha)] + 5 \log r \Delta. \quad (2)$$

Here, we have defined

$$\text{where } \left\{ \begin{array}{l} \Phi_i = W\Phi_{Si} + (1 - W)\Phi_{Li}; \quad i = 1, 2, \\ W = \exp \left[-90.56 \tan^2 \frac{1}{2}\alpha \right], \\ \Phi_{Si} = 1 - \frac{C_i \sin \alpha}{0.119 + 1.341 \sin \alpha - 0.754 \sin^2 \alpha}, \\ \Phi_{Li} = \exp \left[-A_i \left(\tan \frac{1}{2}\alpha \right)^{B_i} \right], \end{array} \right.$$

with the numerical constants such that $A_1 = 3.332$, $A_2 = 1.862$, $B_1 = 0.631$, $B_2 = 1.218$, $C_1 = 0.986$ and $C_2 = 0.238$. The slope parameter G is set to 0.15 corresponding to low-albedo C-type asteroids. C-type are the most common variety of asteroids constituting more than 75% of the Main Belt. They are extremely dark with an albedo of typically 0.03. They are chemically similar to carbonaceous chondritic meteorites (so they have approximately the same composition as the Sun, minus hydrogen, helium and other volatiles).

If the asteroid is seen at zero phase angle at a position where both r and Δ are 1 AU, then its magnitude adjustment vanishes. The formula for the magnitude adjustment ceases to hold when the phase angle exceeds 120°. This happens occasionally in our simulations (for example, for asteroids of the inferior planets). These cases are not included in our synthetic observations. They are quite unimportant from an observational point of view, as the asteroids then lie too close to the Sun to be detected in the visible wavebands. The most useful datum appears to be the average magnitude adjustment at the regions of greatest concentration of co-orbiting asteroids on the plane of the sky. This is calculated for the cloud around each planet, by integrating the distribution of magnitude adjustments at the heliocentric longitude corresponding to greatest surface density.

We typically present our results using contour plots of the probability density distributions in the plane of observables with the colours from blue to red denoting regions

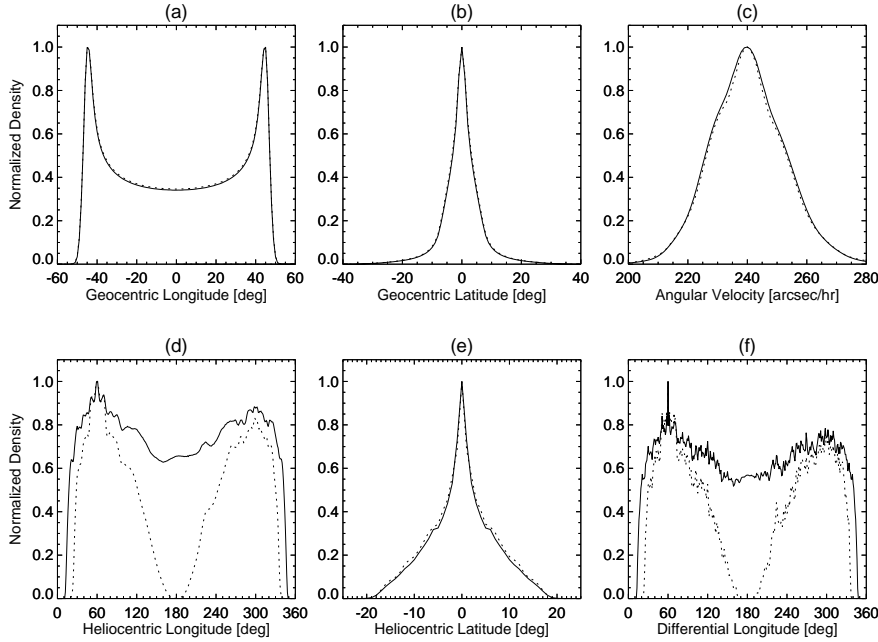


Figure 2. The one-dimensional probability distributions for synthetic observations of coorbiting Venusian asteroids. These are (a) geocentric longitude (b) geocentric latitude, (c) angular velocity, (d) heliocentric longitude, (e) heliocentric latitude and (f) differential longitude. Full lines represent Sample I, dotted lines Sample II.

Quantity	Sample	Mean	FWHM	Minimum	Maximum
XY Angular Velocity	I	$238.8'' \text{ hr}^{-1}$	$28.2'' \text{ hr}^{-1}$	$204'' \text{ hr}^{-1}$	$276'' \text{ hr}^{-1}$
Z Angular Velocity	I	$0.0'' \text{ hr}^{-1}$	$33.9'' \text{ hr}^{-1}$	$-68'' \text{ hr}^{-1}$	$68'' \text{ hr}^{-1}$
Total Angular Velocity	I	$240.4'' \text{ hr}^{-1}$	$27.8'' \text{ hr}^{-1}$	$204'' \text{ hr}^{-1}$	$276'' \text{ hr}^{-1}$
Geocentric Latitude	I	0.0°	6.2°	-25°	25°
Geocentric Longitude	I	$45.0^\circ, -45.0^\circ$	10.4°	-48°	48°
Heliocentric Latitude	I	0.0°	4.7°	-17°	17°
Heliocentric Longitude	I	$60.0^\circ, 299.5^\circ$	325.3°	17°	343°

Table 3. The statistical properties of the one-dimensional distributions of observations for our sample of long-lived coorbiting Venusian asteroids. The mean, full-width half-maximum (FWHM) and 99% confidence limits on the minimum and maximum values are recorded.

from highest to lowest density. We draw contour levels representing points at 90%, 75%, 50%, 25%, 10% and 5% of the peak value. The contour maps always show the unweighted synthetic observations and do not account for the brightness of the test particles. In addition to contour plots, we also provide the one-dimensional distributions of geocentric and heliocentric ecliptic longitude and latitude, differential longitude and total angular velocity. The differential longitude is the difference between the mean synodic longitudes of the test particle and the planet. We have abstracted from our plots some statistics which should prove useful for observational searches. These include the means and the full-width half-maximum (FWHM) spreads of the distributions, as well as 99% confidence limits on the maximum and min-

imum values. The statistics are given in Tables 3, 5, 6 and 7 for Venus, the Earth, Mars and Mercury respectively.

3 VENUS

3.1 Observables

We first discuss the results for Sample I (all survivors). Fig. 1(a) shows the enormous area of sky that these objects can occupy. The 50% contour encloses ≈ 300 square degrees of sky. The distribution is centered around the ecliptic. Note that the orbital plane of Venus, which marks the midplane of the distribution of coorbiting objects, is misaligned with the

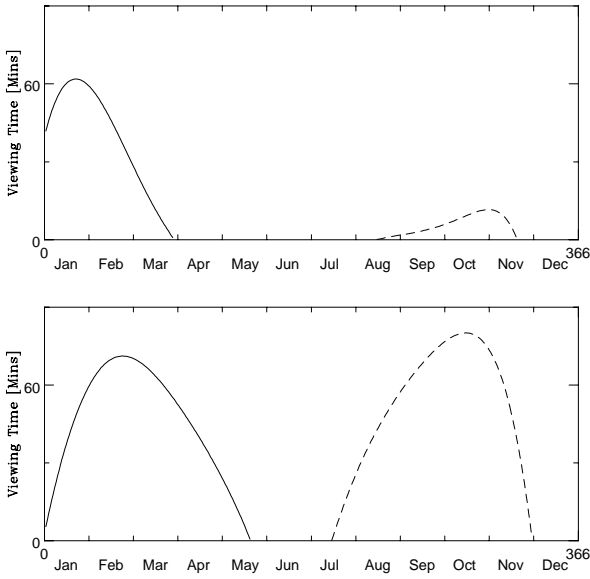


Figure 3. This shows the observing time for the trailing (unbroken line) and leading (broken line) Venusian Lagrange points from (a) Mauna Kea and (b) La Silla observatories for the year 2000.

Planet	Δm_V	R (in km)
Mercury	0.6	–
Venus	1.7	0.8
Earth	2.0	1.0
Mars	3.5	1.9

Table 4. For the asteroidal cloud around each planet, this shows the magnitude adjustment Δm_V at the region of greatest concentration on the sky. The GAIA all-sky survey satellite will scan the triangular Lagrange points of Venus, the Earth and Mars. The magnitude adjustment is used to estimate the radius R of the smallest asteroid detectable by GAIA, assuming the survey is complete to $V \approx 20$.

ecliptic by $\approx 3^\circ$. This accounts for some of the thickness in the latitudinal direction. The highest probability density occurs at geocentric ecliptic longitudes corresponding to Venus' greatest eastern and western elongations. These are at $\ell_g = \pm \arcsin a_V \approx \pm 44^\circ$, where a_V is the semimajor axis of Venus in AU. Fig. 1(b) shows the same distribution in the plane of heliocentric ecliptic longitude and latitude. The distribution is concentrated towards the plane of the ecliptic, but the disk is quite thick. There is an asymmetry evident between the leading L_4 and trailing L_5 points. For L_4 , the probability density has a narrow peak at the classical value of $(\ell_h = 60^\circ, \beta_h = 0^\circ)$, but for L_5 , the peak is broader and runs from $(\ell_h \approx 260^\circ - 310^\circ, \beta_h = 0^\circ)$. In fact, the Jovian Trojans are known to have a markedly asymmetric distribution with $\approx 80\%$ librating about the leading L_4 point. In all our simulations, asymmetries arise because more

of our initial sample of 2000 objects survive the preliminary 1 million year integration about L_4 than L_5 (see Table 2). However, these asymmetries are always rather mild.

The distribution of velocities in the plane of, and perpendicular to, the ecliptic is shown in Fig. 1(c). The velocity dispersion perpendicular to the ecliptic is much larger than the velocity dispersion in the plane. Let us recall that the objects in our sample come from a narrow range of initial semimajor axes corresponding to the coorbital zone. The width of this zone can be deduced from the resonance overlap criterion (Wisdom 1980). By itself, this range in semimajor axes implies a very small scatter in the velocities in the plane, so it is the distribution of eccentricities that is responsible for most of the broadening. As regards the velocity distribution out of the plane, the substantial scatter is largely produced by the range of inclinations. Finally, Fig. 1(d) shows the distribution of magnitude adjustment versus geocentric longitude. The brightest objects occur at $\ell_g \approx 0^\circ$. These are the asteroids at superior conjunction. Even though they are furthest away from the Earth, this is outweighed by the effects of the almost zero phase angle. Of course, this portion is of little observational relevance. The broadest range of magnitude adjustments occurs at the greatest eastern and western elongations $\ell_g \approx \pm 45^\circ$. Here, the phase angle changes quickly for small changes in the longitude. At this point, where the greatest concentration of objects occurs and so is probably of most observational relevance, the typical magnitude adjustment is ≈ 1.7 .

For the case of Venus, the contour plots for Sample II (Trojans alone) are very similar to Sample I – even down to the detailed shapes of the contours. Accordingly, we do not present them here, although they are available in Tabachnik (1999). The only figure that is markedly different is the distribution as seen in the plane of heliocentric longitude and latitude. Obviously, a sample of Trojans do not reach the conjunction point at $\ell_h = 180^\circ$ and so the probability density falls to zero here.

Fig. 2 shows the one-dimensional distributions, while Table 3 gives the means, full-width half-maximum (FWHM) thicknesses, the minima and maxima (at the 99% confidence level) of the distributions. In each case, results are presented for Sample I (full lines) and Sample II (dotted lines). Only in the case of heliocentric ecliptic longitude and differential longitude are there any readily discernable differences between Sample I and Sample II. The distributions in both heliocentric and geocentric ecliptic latitude show that coorbiting Venusian asteroids are most likely to be found in or near to the ecliptic. As regards longitude, the distributions always peak at or close to the classical Lagrange points, but they are broad. The horseshoe orbits in Sample I cause the probability of discovery even at the conjunction points to be far from insignificant. The angular velocity of Venus is $240.4 \text{ arcsec hr}^{-1}$ and this coincides exactly with the mean of the distribution of total angular velocity. However, this distribution, too, is rather broad with a FWHM of $27.8 \text{ arcsec hr}^{-1}$. This hints that it may not be optimum to track the telescope with the expected rate of Venus.

3.2 Strategy

One strategy for finding coorbiting Venusian asteroids is wide-field imaging. Fig. 3 shows the viewing time of the

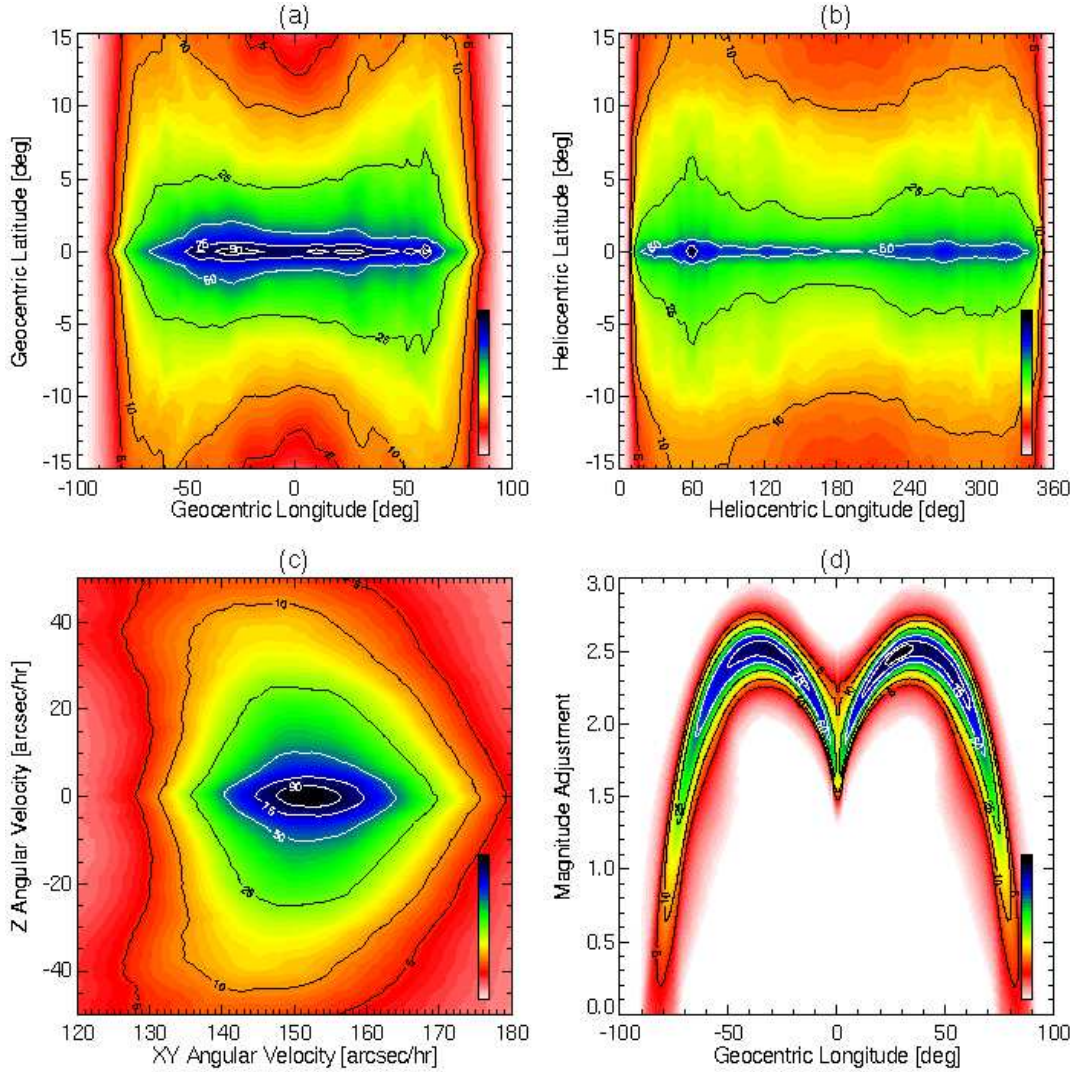


Figure 4. This shows the observable properties of Sample I of long-lived horseshoe and tadpole orbits around the terrestrial Lagrange points. The panels illustrate the probability density in the planes of (a) geocentric ecliptic latitude and longitude, (b) heliocentric ecliptic latitude and longitude, (c) angular velocity in the ecliptic ($X - Y$) versus angular velocity perpendicular (Z) to the ecliptic, and (d) magnitude adjustment versus geocentric longitude.

Venusian Lagrange points as a function of calendar date for the year 2000, tailored for the case of the observatories at Mauna Kea (upper panel) and La Silla (lower panel). The figure is constructed by taking the difference between the moment when the L_5 point reaches 2.5 airmasses and the end of morning civil twilight. In the later months of 2000, only the leading L_4 point is visible and the figure gives the difference between the onset of evening civil twilight and the moment when the L_4 point reaches 2.5 airmasses. This is a very generous definition of observing time, but even so the Venusian Lagrange points are visible in 2000 for, at best, barely more than an hour. In 2000, Venus is visible in the morning sky till the middle of April; it reappears in the evening sky after early August. In the early months of 2000, only the trailing L_5 point is visible, whereas in the later months, only the leading L_4 point is. Venus is below the plane of the ecliptic for all of 2000, and so the southern observatories provide more propitious observing conditions.

For La Silla, the best times are February or March for the L_5 point, and October or November for the L_4 point.

The other major problem is the very fast motions that these objects typically have ($240.4 \text{ arcsec hr}^{-1}$ is the mean for Venusian Trojans). As the velocity distributions are broad, this may hinder techniques such as tracking the camera at the average motion rate and looking for unstreaked objects. It may be better to track the telescope at the side-real rate and use short exposures to minimise trailing loss in candidate Trojans. In any case, it is imperative that discovery of any object happen preferably in real time, but certainly within 24 hours, so that follow-up frames can be obtained as quickly as possible and the candidate is not lost. This necessitates the development of optimised software for real-time analysis (similar to that already used in the Kuiper-Edgeworth Belt searches).

A second strategy for finding coorbiting Venusian asteroids is to exploit the database that will be provided by GAIA. This is an ESA all-sky survey satellite and will pro-

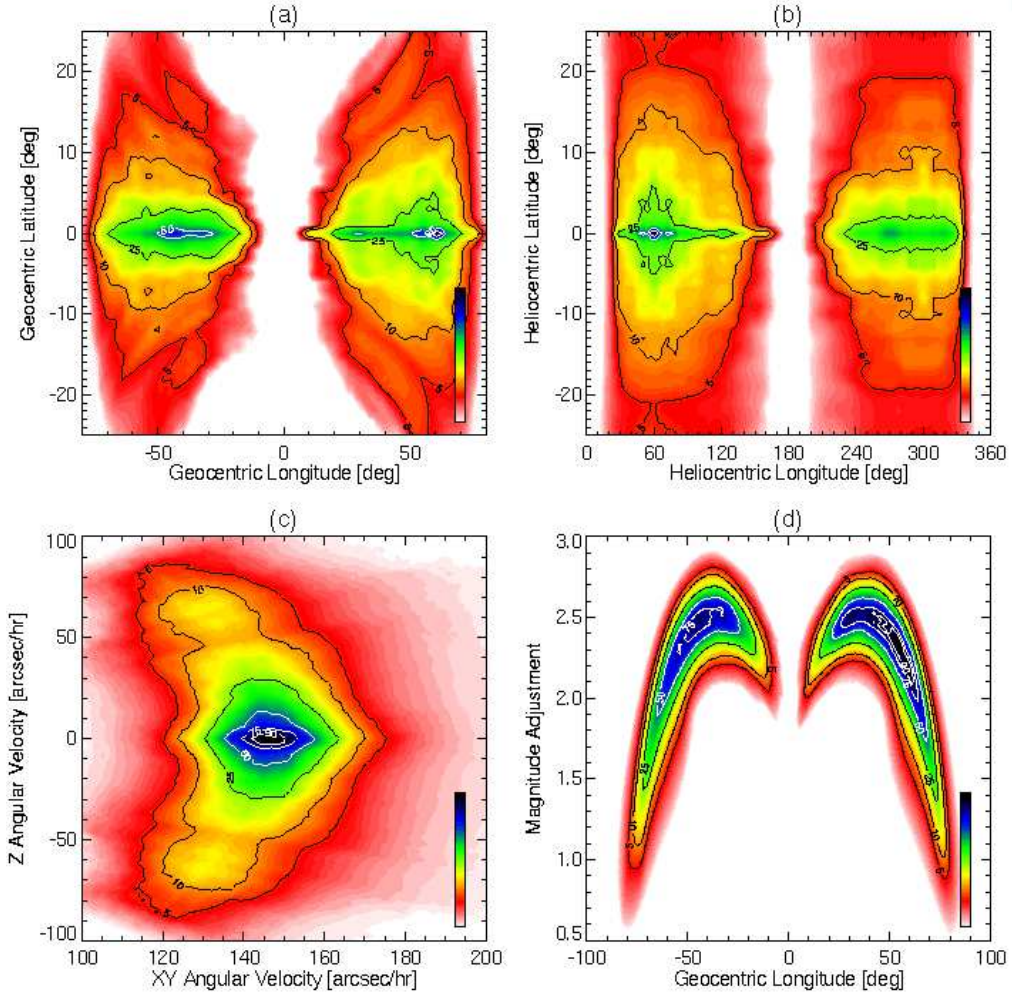


Figure 5. As Fig. 4, but for the sample II (terrestrial Trojans alone).

vide multi-colour and multi-epoch photometry, spectroscopy and astrometry on over a billion objects. The database will be complete to at least $V \approx 20$. GAIA will observe to within 35° of the Sun, so identification of coorbiting asteroidal companions of Venus, the Earth and Mars will be possible. *To our knowledge, this will be the first time the Venusian Lagrange points have ever been scanned.* For each of the planets, Table 4 shows the minimum size C-type asteroid that can be found with GAIA. For the Venusian cloud, asteroids with radii $\gtrsim 0.8$ km can be detected. GAIA will observe each asteroid roughly a hundred times over the mission lifetime. Identification of successive apparitions of the same objects in the database will be possible using estimates of the proper motions. Thanks to the astrometric accuracy of the GAIA satellite, precise orbits for any newly discovered Trojans will be obtained.

4 THE EARTH

4.1 Observables

The Earth is known to have one coorbiting companion, 3753 Cruithne, which follows a temporary horseshoe orbit (Wiegert, Innanen & Mikkola 1997; Namouni, Christou & Murray 1999). Figs. 4 and 5 and shows the observable properties for Samples I (tadpoles and horseshoes) and II (tadpoles only). There are now more substantial differences between the two, and so we give the contour plots for both the samples. The one-dimensional distributions are given in Fig. 6 and some useful statistics in Table 5. Our results can usefully be compared to Wiegert et al. (2000), who also used numerical simulations to derive observable properties of terrestrial Trojans. Our approach differs somewhat from theirs. First, they restricted their study to tadpole orbits. Second, they used a number of plausible hypotheses to set the semi-major axis, inclination and eccentricity limits on their initial population, whereas we have used the results from our lengthy numerical simulations in Paper I. Both approaches seem reasonable, and the differences between our results give an idea of the underlying uncertainties in the problem.

Fig. 4(a) shows the probability distribution in the plane

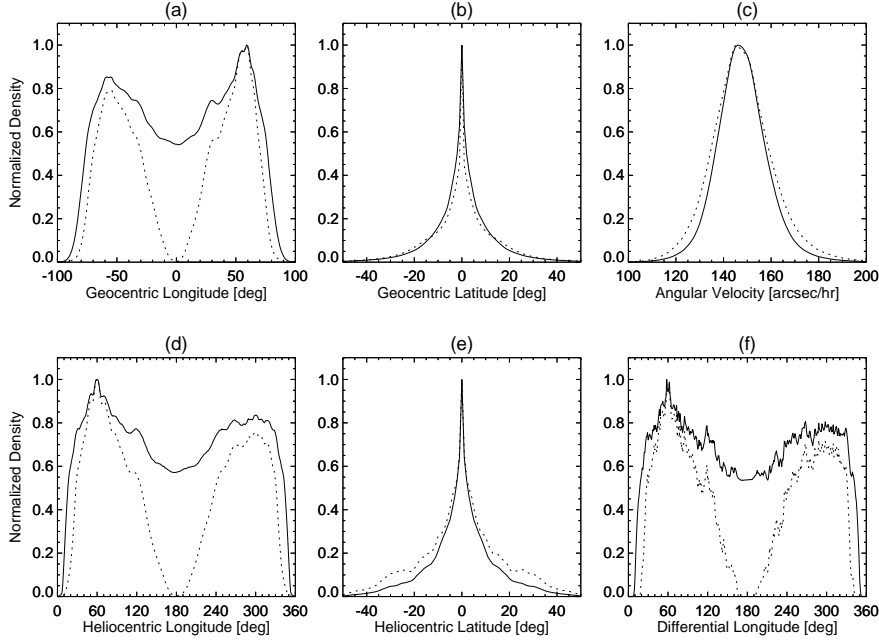


Figure 6. The one-dimensional probability distributions for synthetic observations of coorbiting terrestrial asteroids. These are (a) geocentric longitude (b) geocentric latitude, (c) angular velocity, (d) heliocentric longitude, (e) heliocentric latitude and (f) differential longitude. Full lines represent Sample I, dotted lines Sample II.

Quantity	Sample	Mean	FWHM	Minimum	Maximum
XY Angular Velocity	I	$144.4'' \text{ hr}^{-1}$	$22.5'' \text{ hr}^{-1}$	$109'' \text{ hr}^{-1}$	$179'' \text{ hr}^{-1}$
Z Angular Velocity	I	$0.0'' \text{ hr}^{-1}$	$22.3'' \text{ hr}^{-1}$	$-84'' \text{ hr}^{-1}$	$84'' \text{ hr}^{-1}$
Total Angular Velocity	I	$147.9'' \text{ hr}^{-1}$	$21.0'' \text{ hr}^{-1}$	$113'' \text{ hr}^{-1}$	$181'' \text{ hr}^{-1}$
Geocentric Latitude	I	0.0°	4.0°	-42°	42°
Geocentric Longitude	I	$59.6^\circ, -59.7^\circ$	153.4°	-84°	84°
Heliocentric Latitude	I	0.0°	5.0°	-42°	42°
Heliocentric Longitude	I	$60.0^\circ, 299.5^\circ$	328.1°	13°	347°
XY Angular Velocity	II	$142.8'' \text{ hr}^{-1}$	$28.3'' \text{ hr}^{-1}$	$102'' \text{ hr}^{-1}$	$182'' \text{ hr}^{-1}$
Z Angular Velocity	II	$0.0'' \text{ hr}^{-1}$	$27.3'' \text{ hr}^{-1}$	$-88'' \text{ hr}^{-1}$	$88'' \text{ hr}^{-1}$
Total Angular Velocity	II	$147.9'' \text{ hr}^{-1}$	$25.1'' \text{ hr}^{-1}$	$108'' \text{ hr}^{-1}$	$186'' \text{ hr}^{-1}$
Geocentric Latitude	II	0.0°	1.8°	-43°	43°
Geocentric Longitude	II	$59.3^\circ, -59.3^\circ$	153.4°	-84°	84°
Heliocentric Latitude	II	0.0°	5.19°	-17°	17°
Heliocentric Longitude	II	$60.0^\circ, 299.5^\circ$	90°	27°	333°

Table 5. The statistical properties of the synthetic observations of our samples of long-lived coorbiting terrestrial asteroids. As usual, Sample I is all surviving asteroids, Sample II is tadpoles only.

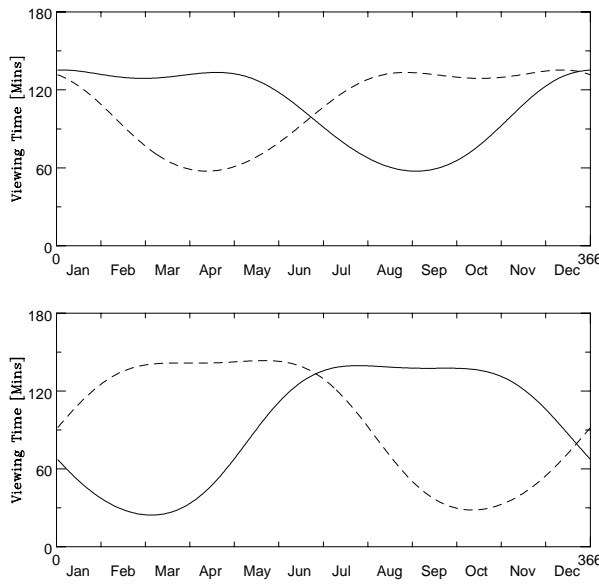


Figure 7. This shows the observing time for the trailing (unbroken line) and leading (broken line) terrestrial Lagrange points from (a) Mauna Kea and (b) La Silla observatories for the year 2000.

of geocentric ecliptic longitude and latitude for Sample I. The 50% contour encompasses some 350 square degrees of sky, so a huge area has to be surveyed for coorbiting asteroids. Even if the search is restricted to tadpoles or Trojans, Fig. 5(a) shows that the 50% contour encloses some 30 square degrees of sky. Figs. 4 and 5 also show the concentration of objects in the plane of heliocentric ecliptic longitude and latitude. As in the case of Venus, there is an asymmetry between leading and trailing points. This is because more of the initial population around the L_4 point survive the 1 million year integration. Of course, exact symmetry between L_4 and L_5 is not expected because of differences in the planetary phases. For neither Sample I nor Sample II does the greatest probability density occur at the classical values of ($\ell_g = \pm 60^\circ, \beta_g = 0^\circ$), but at smaller geocentric ecliptic longitudes. This effect was already noticed by Wiegert et al. (2000), who argued that the highest concentration of Trojans in the sky occurs at ($\ell_g \approx \pm 55^\circ, \beta_g = 0^\circ$). The physical reason for this is that test particles on both tadpole and horseshoe orbits spend more time in the elongated tail. Even so, the effect is slight; the one-dimensional probability distributions displayed in Fig. 6 show that, when integrated over all latitudes, the maxima return to the classical values of $\ell_g = \pm 60^\circ$. Note that the thickness in the heliocentric ecliptic latitudinal direction seems larger for the Venusian cloud than for the terrestrial (compare Fig. 1(b) with Fig. 4(b)). This seems surprising, as the stable coorbiting satellites persist to much higher inclinations in the case of the Earth as compared to Venus. The reason is geometric, as the Earth is further from the Sun than Venus. In actual distances, the FWHM thickness of the terrestrial asteroids is ≈ 0.09 AU, while for the Venusian asteroids, it is ≈ 0.06 AU. This is as expected, since the terrestrial distribution has a tail extending to higher latitudes.

Figs. 4(c) and 5(c) show the distributions generated by Samples I and II respectively in the plane of velocities. The Earth has a mean motion of 147.84 arcsec hr^{-1} , very close to the mean total angular velocity of both Samples I and II. However, the distribution of velocities is broad, with a FWHM of exceeding 20 arcsec hr^{-1} (see Table 5). Again, this calls into question the applicability of the search strategies which take two or three exposures of each field while tracking the telescope at a rate of 150 arcsec hr^{-1} along the ecliptic (c.f., Whiteley & Tholen 1999). This is only effective if the distribution of expected longitude rates is very narrow. If the coorbiting objects possess broad distributions of angular motions, then, with this technique, not only are background stars trailed, but so are the candidate objects (unless they are moving at exactly the right rate). This renders detection very difficult.

The magnitude adjustment distributions are shown in Figs. 4(d) and 5(d). For Venus, the nearby asteroids are among the faintest. The converse is true for the Earth. The nearby objects with semimajor axes slightly greater than the Earth's benefit both from small phase angles and small geocentric distances and so are brightest (as also noted by Wiegert et al. 2000). The asteroids at the Lagrange points in Sample I are on average ≈ 2.0 magnitudes fainter than their absolute magnitudes. This number changes only slightly to 2.1 magnitudes for the tadpole-only Sample II. For the same distribution of absolute magnitudes, the Venusian asteroidal cloud is actually brighter than the terrestrial cloud by ≈ 0.3 magnitudes at their respective regions of greatest concentration.

4.2 Strategy

Observational searches for coorbiting terrestrial asteroids present less severe difficulties than the case of Venus, though they are still not easy. Fig. 7 shows the windows of opportunity for the terrestrial Trojans at Mauna Kea (upper panel; c.f., Whiteley & Tholen 1998) and La Silla (lower panel). For the Earth's leading Lagrange cloud, the figure is constructed by calculating the time difference between the beginning of evening civil twilight and the moment when the setting L_5 point reaches 2.5 airmasses. For the Earth's trailing cloud, it is calculated by taking the difference between the the moment when the rising L_4 point reaches 2.5 airmasses and then end of morning civil twilight. Observations can proceed more leisurely than for the Venusian Lagrange points as, during times of peak visibility, there are about 2 hours of viewing time at both Mauna Kea and La Silla. For La Silla, the best times are February to June for the L_5 point, and August to November for the L_4 point.

Unlike Venus, the Earth's Lagrange points have already been the subject of previous scrutiny. The most thorough survey to date is that of Whiteley & Tholen (1999), who scanned some 0.35 square degrees near the L_4 and L_5 points to a limiting magnitude $R \approx 22.8$ without success using a 2048×2048 mosaic camera. By comparison, let us recall from Fig. 5(a) that the 50% contour encloses some 30 square degrees for Sample II of Trojans alone. Whiteley & Tholen tracked the camera at the average motion rate of 148 arcsec hr^{-1} for coorbiting terrestrial asteroids, taking generally two, occasionally three, 300s exposures of each field. Assuming a typical seeing of 0.8 arcsec, then any object with

motions in the range $\approx 143 - 153$ arcsec hr^{-1} will move less than the seeing during the two exposures. Only these objects will not appear streaked. Using our velocity distributions in Fig. 6, we estimate that such objects comprise only about 35% of our sample. The actual efficiency of Whiteley & Tholen's technique is harder to estimate, as it depends on the details of its implementation, but it seems likely that it is $\lesssim 50\%$.

There are also earlier photographic plate surveys, which covered larger areas of sky, but with much less sensitivity. For example, Dunbar & Helin (1983) took sixteen Schmidt plates near the L_4 point, though only two near the L_5 point, with the 1.2m Palomar telescope. They claim that the number of terrestrial Trojans with an absolute magnitude $H_V \lesssim 20$ around L_4 must be $\lesssim 10$. Neglecting phase angle effects, the radius of an object given its absolute magnitude H_V is roughly

$$R \approx 10^{0.2(m_{V,\odot} - H_V)} \quad (\text{in AU}). \quad (3)$$

Taking the apparent visual magnitude of the Sun $m_{V,\odot}$ as -26.77 (Lang 1980), this becomes

$$R \approx 3.8 \times 10^3 \left(\frac{0.03}{p_v} \right)^{\frac{1}{2}} 10^{-0.2H_V} \quad (\text{in km}), \quad (4)$$

where p_v is the V band geometric albedo. Let us assume $p_v = 0.03$, as is reasonable for dark C-type asteroids (e.g., Zellner 1979). Then, Dunbar & Helin's (1983) claim is that there are at most ten objects with $R \gtrsim 0.4$ km around L_4 . Suppose the number of objects with radii greater than R can be approximated by a power law

$$N(> R) \propto R^{1-q}. \quad (5)$$

Taking $q \approx 3$, as suggested by studies of C-type main belt asteroids in Zellner (1979), then $N(> 0.1 \text{ km}) \approx 160$ around L_4 . It is clear that the observational constraints on the existence of a few bright or many faint coorbiting terrestrial asteroids are rather weak.

5 MARS

5.1 Observables

Our sample of coorbiting Martian asteroids is composed solely of inclined tadpole orbits. In Paper I, we found that asteroids in the orbital plane of Mars are unstable and do not survive on 60 Myr timescales. Without the range of semi-major axes provided by our in-plane surveys, our procedure for generating initial conditions gives only tadpoles.

Fig. 8(a) and (b) shows that the greatest concentration of Trojans lies above the ecliptic, at $(\ell_g = 0^\circ, \beta_g \approx \pm 9^\circ)$ or $(\ell_h = 60^\circ, \beta_h \approx \pm 12^\circ)$. Interestingly, the two known Martian Trojans (5261 Eureka and 1998 VF31) were discovered by opposition searches close to the ecliptic. The discoveries were serendipitous, insofar as the surveys were directed towards finding Near-Earth Objects. In fact, the probability density in the ecliptic is typically 50% of the peak. It is surely encouraging that search strategies that are far from optimum have already yielded success. Compared to our earlier Figs 1 and 4 for Venus and the Earth, the regions of high probability density extend to much higher latitudes in the case of Mars. Of course, this is a consequence of the

fact that the stable Trojans survive only for starting inclinations between 14° and 40° (see Paper I). As the sample contains only tadpoles, the probability density falls to zero at the conjunction points ($\ell_h \approx 180^\circ$). In heliocentric longitude, the greatest concentration lies close to the classical Lagrange point values of $\ell_h \approx 60^\circ$ and 300° . The maximum in geocentric longitude occurs at $\ell_g = 0^\circ$. This is of course a purely geometric effect, as the Martian asteroids are here most distant from the Earth. Angular distances correspond to larger true distances and so the sampling, which proceeds at equal time instants, gives a higher concentration.

The mean motion of Mars is 78.6 arcsec hr^{-1} . However, as shown in Fig. 8(c), the maximum of the probability distributions occurs at a velocity of ≈ 65 arcsec hr^{-1} in the plane of the ecliptic and a velocity of $\approx \pm 15$ arcsec hr^{-1} perpendicular to the ecliptic. Evident in the contour plot are wakes of high concentration regions behind the twin peaks of the maxima, which persist to quite high velocities. This structure is a consequence of the unusual range of inclinations that long-lived coorbiting Martian asteroids must possess. The distribution of total angular velocity is shown in Fig. 9 and is strikingly asymmetric. We have checked that the average of this distribution is indeed the same as the mean motion of Mars, as it should be. The largest velocities occurs when the test particles are sampled near perihelion, the smallest velocities when the test particles are sampled near aphelion. Although there is a pronounced peak in the probability distribution corresponding to the velocities at aphelion, there is no peak corresponding to perihelion, but rather a long tail. This happens because the sampling is at equal time intervals and so – as any orbit spends most time at aphelion – this feature is accentuated. There is a mild secondary peak in the one-dimensional distribution at ≈ 87 arcsec hr^{-1} . We suspect that this is caused by the wakes and so is a consequence of the range of inclinations (c.f. the case of Mercury).

The probability density is shown in the plane of magnitude adjustment versus angular velocity in Fig. 8(d). The brightest objects are the ones closest to us because of the advantageous distance and phase angle effects. They are found at typical heliocentric ecliptic longitudes of $-20^\circ \lesssim \ell_h \lesssim 20^\circ$. The brightest objects are moving faster than average (compare, for example, the 50% contours in Fig. 8(c) and (d)). At the regions of greatest concentration ($\ell_h = 60^\circ, \beta_h \approx \pm 12^\circ$), the average magnitude adjustment is ≈ 3.5 .

The one-dimensional probability distributions are shown in Fig. 9. The most interesting features are the broadness of the distributions in velocity and in latitude. The FWHM of the double-peaked latitudinal distributions recorded in Table 6 refers to the width about the peaks. The total FWHM of these double-peaked distributions is of course far broader, something like $\approx 60^\circ$. The distribution in differential longitude may be compared with our earlier presentation, using a different sample, in Tabachnik & Evans (1999). There, we found that the L_5 peak was larger than the L_4 , whereas here the reverse is the case. This cautions us against reading too much into the mild asymmetries present in our results. Stability arguments certainly can produce such slight differences between L_4 and L_5 . However, if there are any large asymmetries in the data, it seems that these must be produced by other mechanisms (such as plan-

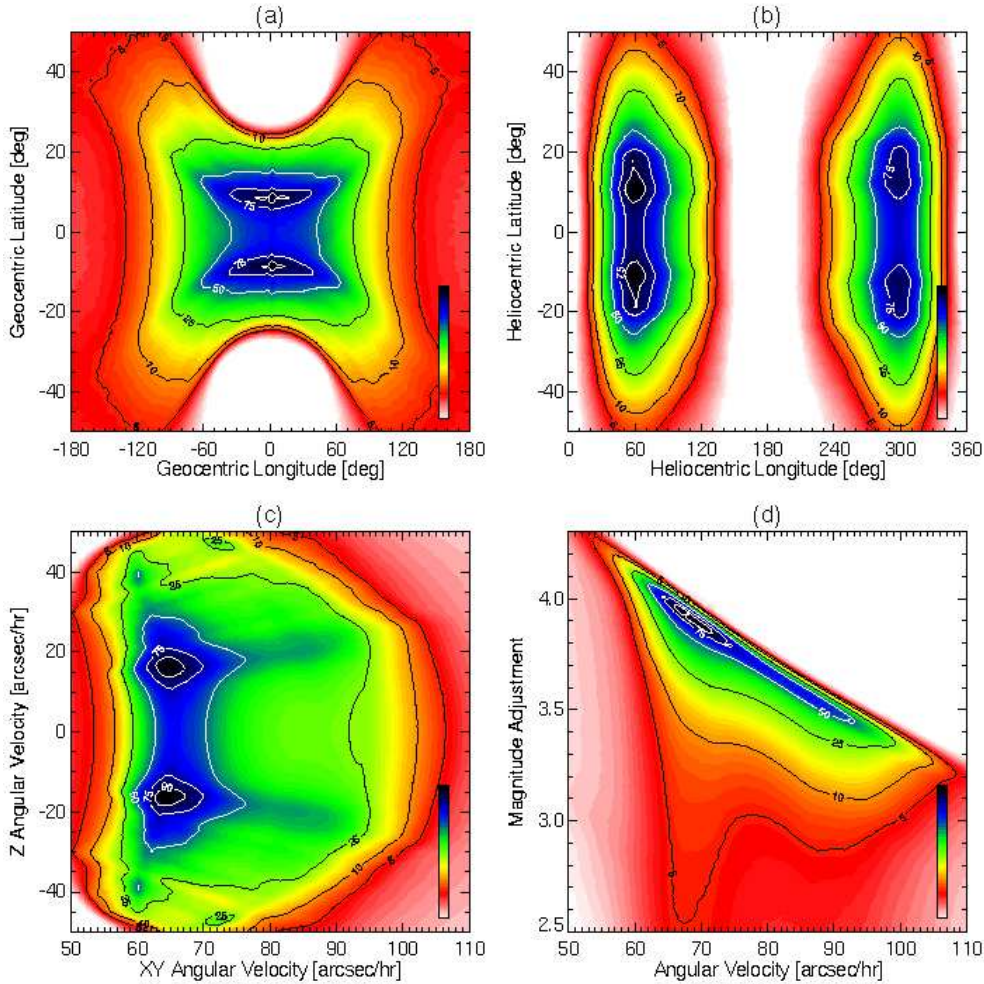


Figure 8. This shows the observable properties of Sample II of long-lived tadpole orbits around the Martian Lagrange points. The panels illustrate the probability density in the planes of (a) geocentric ecliptic latitude and longitude, (b) heliocentric ecliptic latitude and longitude, (c) angular velocity in the ecliptic ($X - Y$) versus angular velocity perpendicular (Z) to the ecliptic, and (d) magnitude adjustment versus geocentric longitude.

Quantity	Sample	Mean	FWHM	Minimum	Maximum
XY Angular Velocity	II	$74.8'' \text{ hr}^{-1}$	$27.0'' \text{ hr}^{-1}$	$52'' \text{ hr}^{-1}$	$116'' \text{ hr}^{-1}$
Z Angular Velocity	II	$0.0'' \text{ hr}^{-1}$	$69.2'' \text{ hr}^{-1}$	$-51'' \text{ hr}^{-1}$	$51'' \text{ hr}^{-1}$
Total Angular Velocity	II	$78.8'' \text{ hr}^{-1}$	$32.2'' \text{ hr}^{-1}$	$54'' \text{ hr}^{-1}$	$114'' \text{ hr}^{-1}$
Geocentric Latitude	II	0.0°	43.4°	$\lesssim -50^\circ$	$\gtrsim 50^\circ$
Geocentric Longitude	II	-0.2°	197.7°	-180°	180°
Heliocentric Latitude	II	0.0°	53.6°	$\lesssim -50^\circ$	$\gtrsim 50^\circ$
Heliocentric Longitude	II	$60.0^\circ, 299.5^\circ$	$53.8^\circ, 49.7^\circ$	$\lesssim 10^\circ$	$\gtrsim 350^\circ$

Table 6. The statistical properties of the synthetic observations of our samples of long-lived coorbiting Martian asteroids. Sample II is tadpoles only.

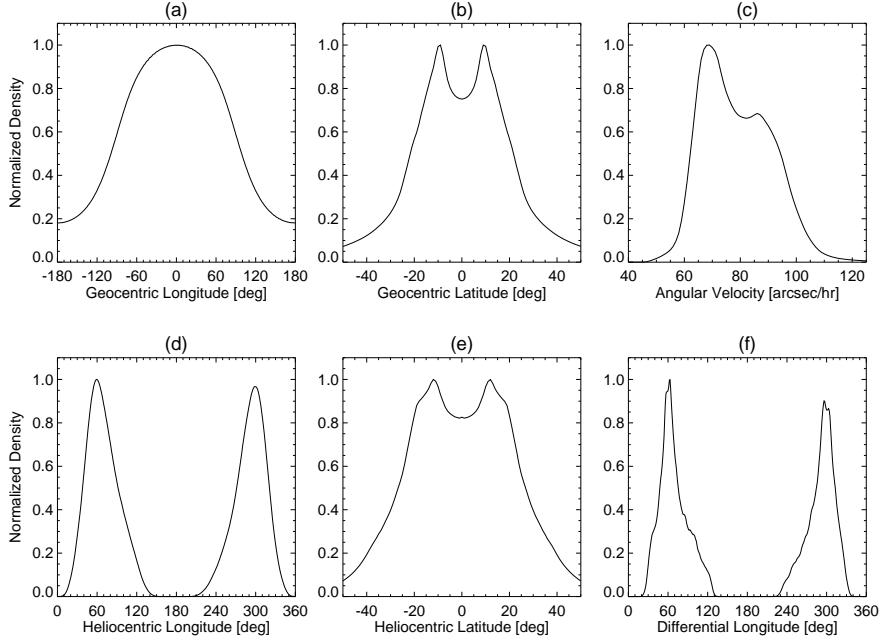


Figure 9. The one-dimensional probability distributions for synthetic observations of coorbiting Martian asteroids. These are (a) geocentric longitude (b) geocentric latitude, (c) angular velocity, (d) heliocentric longitude, (e) heliocentric latitude and (f) differential longitude.

etary migrations). Both the known Martian Trojans librate about L_5 , and it will be interesting to see if this trend is maintained with further discoveries.

5.2 Strategy

As Mars is a superior planet, the observational strategy for Trojan searches is very considerably eased. The main reason why only two Martian Trojans are known is that the optimum locations to scan are at geocentric ecliptic latitudes of $\pm 9^\circ$ or, equivalently, heliocentric ecliptic latitudes of $\pm 12^\circ$. Most survey work is concentrated within a few degrees of the ecliptic itself. In fact, both 5261 Eureka and 1998 VF31 were discovered when their orbits took them close to the ecliptic (see Holt & Levy 1990; *Minor Planet Circular 33763*).

1998 VF31 was discovered by *The Lincoln Near Earth Asteroid Research Project* (LINEAR, see “<http://www.ll.mit.edu/LINEAR/>”). LINEAR uses a 2560×1960 pixel CCD camera to search to a limiting magnitude of ≈ 19.5 for Near-Earth Objects (NEOs). It has discovered over one hundred NEOs in 1999 alone. The main search strategy is to look near solar opposition and around the ecliptic. LINEAR probably provides the best existing constraints on numbers of objects at the Martian Lagrange points. The Trojan 1998 VF31 has absolute magnitude $H_V = 17.1$ (see “<http://cfa-www.harvard.edu/iau/lists/MarsTrojans.html>”). From its magnitude, 1998 VF31 has a radius of ≈ 1.4 km. Let us assume that LINEAR has surveyed the Martian L_5 point complete to 17th magnitude. This is probably not the case, but our assumption then yields an underestimate for the to-

tal population. Assuming Poisson statistics, then at the 99.9 % confidence level, there can be at most seven objects with $z \gtrsim 1.4$ km at the L_5 point. Making the same assumptions as for the terrestrial Trojans (eq. 5), this suggests that the number of objects with radii greater than 0.1 km orbiting around the Martian L_5 point is ≈ 1000 . Of course, caution should be exercised here, as this is a crude estimate. LINEAR can go as deep as $V \approx 19.5$, which suggests that more Martian Trojans can be expected from them soon.

There are two forthcoming surveys that may also provide Martian Trojans. First, *The Sloan Digital Sky Survey* (SDSS) takes multi-colour photometry in the r' , i' , z' , u' and g' bands. It is not an all-sky survey, being limited to latitudes well away from the Galactic plane ($|b| > 30^\circ$) and to ecliptic longitudes around solar opposition ($100^\circ \lesssim \ell_h \lesssim 280^\circ$). Of the terrestrial planets, SDSS can only look for Martian Trojans. These may be provisionally identified by colours, being bright in r' and i' and faint in the other three bands, together with an estimate of their proper motion. If new objects are identified in real time (or nearly so) with SDSS, then immediate ground-based follow-up will permit accurate orbit determination to ensure that they are not lost. Second, the space satellite GAIA will provide an all-sky census of solar system objects, complete to $V \approx 20$ and free from directional biases. This is much needed. The most complete survey of the solar system remains that of Tombaugh (1961), which covered a large fraction of the northern sky to approximately 18th magnitude. Kowal's (1979) survey goes three magnitudes deeper, but is concentrated around the ecliptic. Kowal's main aim was to find slow-moving objects, so his survey does not follow up objects with motions greater than

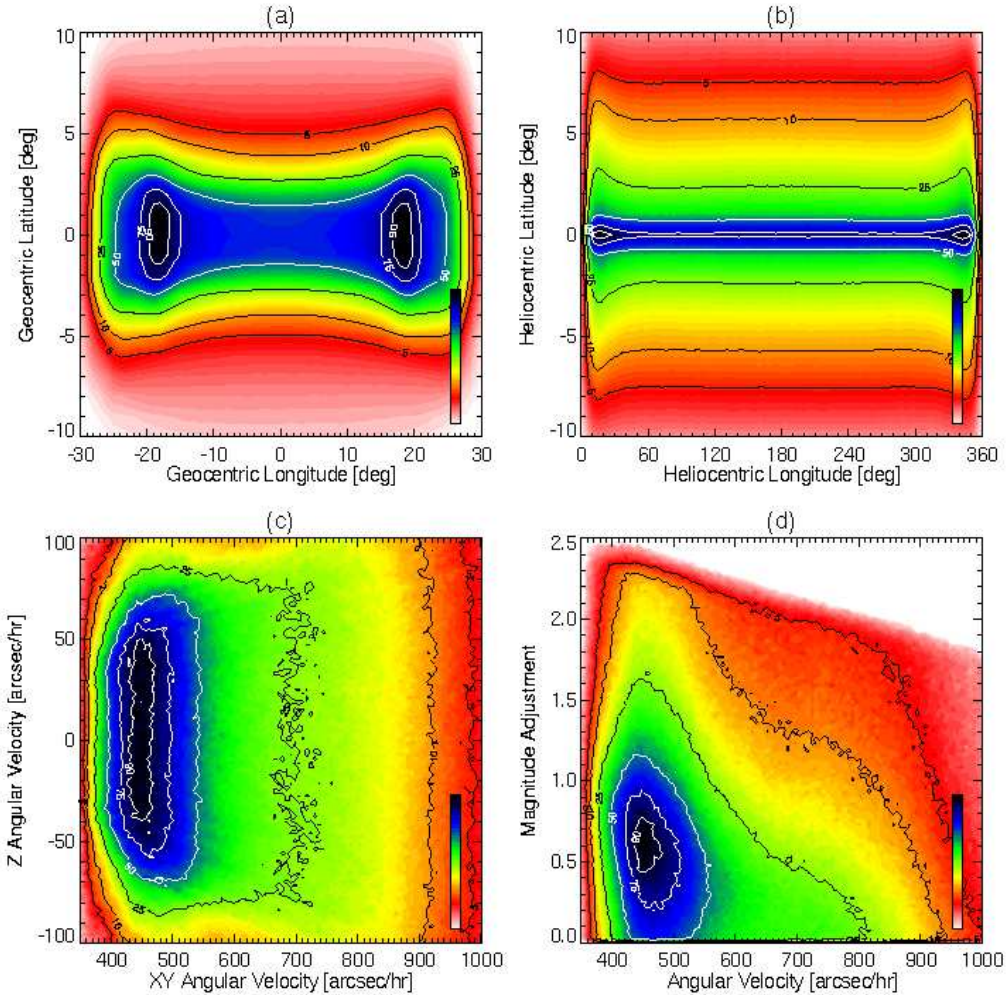


Figure 10. This shows the observable properties of Sample I of long-lived horseshoe orbits around the Mercurian Lagrange points. The panels illustrate the probability density in the planes of (a) geocentric ecliptic latitude and longitude, (b) heliocentric ecliptic latitude and longitude, (c) angular velocity in the ecliptic ($X - Y$) versus angular velocity perpendicular (Z) to the ecliptic, and (d) magnitude adjustment versus geocentric longitude.

15 arcsec hr^{-1} (like Martian Trojans, amongst others). In other words, GAIA will give the most complete catalogue of solar system objects out of the plane of the ecliptic. It will be particularly valuable for objects like Martian Trojans, whose distribution is biased out of the ecliptic. Using our estimate of the average magnitude adjustment at the most favoured location ($\ell_h = 60^\circ$, $\beta_h \approx \pm 12^\circ$), we reckon that GAIA will be sensitive to C-type Martian Trojans with a radius of 1.9 km or greater (see Table 4).

6 MERCURY

6.1 Observables

The case of coorbiting Mercurian asteroids is the most demanding of all. The results of Paper I show that there is a long-lived population of horseshoes with starting differential longitudes very close to Mercury. This stable region is smaller than that of any of the other terrestrial planets.

The procedure used to generate the synthetic observables in the case of Mercury is different from the other three terrestrial planets. The sample of initial conditions is more strictly based on the results of Paper I. The initial semi-major axis and differential longitudes are determined from Figure 4 of Paper I. Then, at each differential longitude, an inclination is randomly chosen between 0° and 10° . The remaining three orbital elements are inherited from the parent planet. Of course, this set of initial conditions contains a minor fraction of test particles which rapidly evolve on chaotic orbits (eventually entering the sphere of influence of a planet or becoming hyperbolic). So, we integrate the system for 1 Myr and then retain only the bodies that survive. The reason for this difference in procedure is that the stable zones of Figure 4 of Paper I are particularly rich in structure, which we wished to retain as far as possible.

The distributions of synthetic observables are shown in Fig. 10. There are a number of points of interest. First, as is evident from Figs. 10(a) and (b), these objects are found

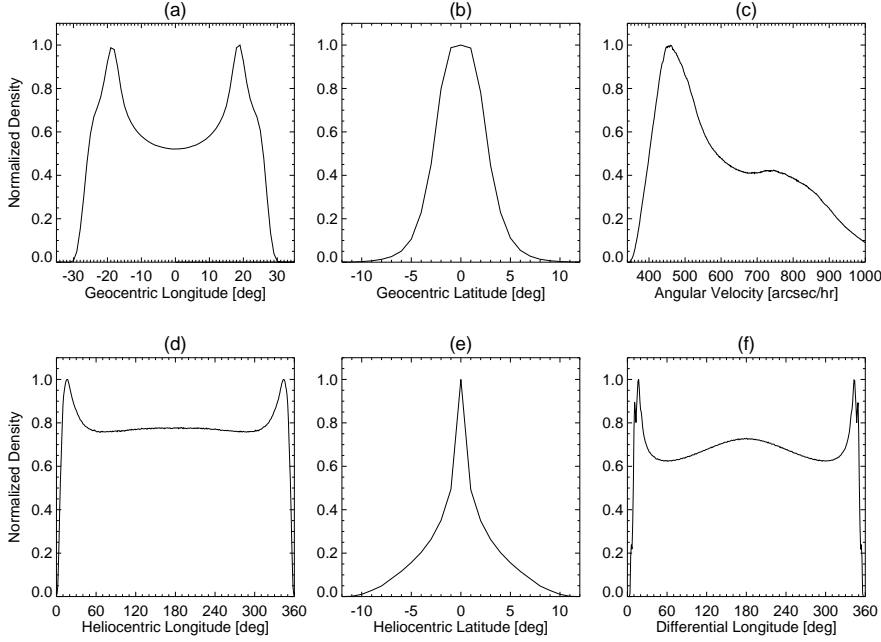


Figure 11. The one-dimensional probability distributions for synthetic observations of coorbiting Mercurian asteroids. These are (a) geocentric longitude (b) geocentric latitude, (c) angular velocity, (d) heliocentric longitude, (e) heliocentric latitude and (f) differential longitude.

Quantity	Sample	Mean	FWHM	Minimum	Maximum
XY Angular Velocity	I	$591'' \text{ hr}^{-1}$	$172.9'' \text{ hr}^{-1}$	$364'' \text{ hr}^{-1}$	$976'' \text{ hr}^{-1}$
Z Angular Velocity	I	$0.3'' \text{ hr}^{-1}$	$170.4'' \text{ hr}^{-1}$	$\lesssim -100'' \text{ hr}^{-1}$	$\gtrsim 100'' \text{ hr}^{-1}$
Total Angular Velocity	I	$459'' \text{ hr}^{-1}$	$186.5'' \text{ hr}^{-1}$	$\lesssim 350'' \text{ hr}^{-1}$	$\gtrsim 1000'' \text{ hr}^{-1}$
Geocentric Latitude	I	0.0°	5.7°	-7°	7°
Geocentric Longitude	I	$18.5^\circ, -18.9^\circ$	51.5°	-28°	28°
Heliocentric Latitude	I	0.0°	2.0°	-9°	9°
Heliocentric Longitude	I	$16.0^\circ, 343.5^\circ$	348.5°	6°	354°

Table 7. The statistical properties of the synthetic observations of our samples of long-lived coorbiting Mercurian asteroids. Sample I is horseshoes only.

very close to the Sun. The greatest elongation of Mercury is at $\ell_g = \pm \text{asina}_M = \pm 22.8^\circ$, where a_M is the semimajor axis of Mercury in AU. But, the maximum concentration of coorbiting asteroids is at somewhat smaller longitudes, $\ell_g = \pm 18^\circ$. Similarly, in heliocentric longitude, the maxima occur at $\ell_h = 16.0^\circ$ and 348.5° and so are rather significantly displaced from the classical values. The unfortunate effect of this is to make the objects still harder to detect, as they are even closer to the Sun than naive reasoning suggests.

Perhaps the most remarkable plot is Fig. 10(c) which shows broad distributions extending to very high velocities indeed. The 99 % confidence limits show that the velocities in the plane of the ecliptic extends from $364 \text{ arcsec hr}^{-1}$ to $976 \text{ arcsec hr}^{-1}$, whereas the velocities perpendicular to the

ecliptic stretch from $-100 \text{ arcsec hr}^{-1}$ to $100 \text{ arcsec hr}^{-1}$. The highest velocities of course occur at perihelion. The reason why such an enormous range of velocities is possible is the eccentricity fluctuations of Mercury, and hence the coorbiting population, during the course of the simulation. Of course, the largest velocities occur at perihelion for the most eccentric orbits. The one-dimensional velocity distribution is shown in Fig. 11. Again, there is a sharp peak corresponding to the velocities at aphelion, whereas the higher velocities are spread out into a long tail. There is a hint of a secondary maximum, although it is not as pronounced as in the case of Mars. The properties of the velocity distribution also conspire against discovery, as these very fast moving objects are extremely hard to locate. Fig. 10(d)

shows the probability distribution in the plane of magnitude adjustment and velocity. The brightest objects occur close to the Sun, at geocentric longitudes $\ell_g \approx 0^\circ$. These are the asteroids close to the conjunction point, which benefit from the almost zero phase angle. A more relevant observational quantity is the typical magnitude adjustment at the region of greatest concentration, which is 0.6.

6.2 Strategy

The Mercurian Lagrange points are always at more than 2.5 airmasses between the hours of twilight, so that searches are not feasible in the visible wavebands. Given the difficulties, it comes as a surprise to find any attempt has been made at this awkward problem. In fact, both Leake et al. (1987) and Campins et al. (1996) have searched for intra-Mercurial objects, the “Vulcanoids” (see Weidenschilling 1978; Evans & Tabachnik 1999), during the day in the infrared L band. Campins et al. (1996) mention plans to look for Mercurian Trojans explicitly. The proximity of coorbiting Mercurian asteroids to the Sun causes them to be hot. The search strategy exploits the fact that they have a substantial component of infrared emission. At ≈ 3.5 microns, the background brightness of the daytime sky is near its minimum, but the thermal emission from the Earth’s atmosphere is still comparatively low. This rationale suggests that the L band, or possibly the K band, offer the best hopes for the searches. Leake et al. (1987) searched between $9^\circ \leq |\ell_g| \leq 12^\circ$ and $|\beta_g| < 1^\circ$. Their main motivation was to find Vulcanoids rather than Trojans, and – as can be seen from Figs. 10 and 11 – this location is not the region of highest concentration of coorbiting asteroids. Nonetheless, the probability density is still significant, being $\approx 60\%$ of the peak. It would be worthwhile to repeat Leake et al.’s (1987) experiment, but using fields of view centered on $(\ell_g = \pm 18^\circ, \beta_g = 0^\circ)$.

Since Leake et al.’s (1987) investigation, the physical size of infrared arrays has increased a lot, but on telescopes the emphasis has been on improving the sampling of the images rather than on increasing the field of view. So, 256×256 InSb arrays are now available but with fields of only about 80×80 arcsec (e.g., NSFCAM on *The Infrared Telescope Facility* (IRTF); see “<http://irtf.ifa.hawaii.edu/>”). A number of larger arrays are just being commissioned, but they tend to be Hg/Cd arrays with less sensitivity in L band than the In/Sb arrays. NSFCAM has a limiting magnitude in L of 13.9; it is unclear whether this deep enough for Mercurian asteroid searches.

There are also some relevant, older searches for faint objects close to the Sun and for sun-grazing comets using solar eclipse photography (Courten 1976). These yielded possible, but unconfirmed, detections of minor bodies. These old searches extend down to approximately 9th magnitude and cover fields of view of $15^\circ \times 15^\circ$ centered on the Sun. A strategy exploiting more up-to-date technology is to use spaceborne coronagraphs. Although only a handful of sun-grazing comets have ever been discovered from the ground, the Large Angle Spectrometric Coronagraph (LASCO) on SOHO (see, “<http://sohowww.nascom.nasa.gov>”) has already discovered several hundred since beginning operation in 1995. Spaceborne instruments are evidently advantageous over ground-based for searches in the infrared, as the problem of thermal emission from the Earth’s atmosphere is side-stepped.

LASCO can detect objects that pass within a projected distance of 30 solar radii, or ≈ 0.15 AU. This corresponds to geocentric ecliptic latitudes satisfying $|\ell_g| \lesssim 9^\circ$. As Fig. 10(a) illustrates, the concentration of coorbiting Mercurian asteroids is not negligible within this region, being $\approx 50\%$ of maximum

7 CONCLUSIONS

This paper has presented synthetic observations for long-lived clouds of coorbiting asteroids around each of the terrestrial planets. Our earlier numerical integrations from Tabachnik & Evans (2000) confirm that some of these objects can survive for timescales up to 100 Myrs, and probably longer still. For Venus and the Earth, we have investigated two samples – one containing both tadpole and horseshoe orbits, the other just tadpole or true Trojan orbits. For Mars, our sample contains only tadpoles; for Mercury, only horseshoes. The observable distributions in geocentric and heliocentric latitude and longitude have been calculated, as well as their typical velocities and magnitudes. All these should be valuable aids in the observational searches for these objects. We briefly summarise our main results for each planet in turn:

(1) For Venus and the Earth, the greatest concentration of objects on the sky occurs close to the classical Lagrange points at heliocentric ecliptic longitudes of 60° and 300° . The distributions are broad, especially if horseshoes are present in the sample. The full-width half maximum (FWHM) in heliocentric longitude for Venus is 325° and for the Earth is 328° . In other words, truly huge areas of sky have to be searched for these objects. The mean and most common velocity of these coorbiting satellites coincides with the mean motion of the parent planet, but again the spread is broad with a FWHM for Venus of 27.8 arcsec hr $^{-1}$ and for the Earth of 21.0 arcsec hr $^{-1}$. The terrestrial Lagrange points have been searched with Schmidt plates and CCD cameras, but these searches cover only small fields of view and rule out large bodies only. As the velocity distributions of the coorbiting population are broad, one possible strategy is to use wide field CCD imaging, tracking the camera at the sidereal rate and using short exposures to minimise trailing loss in the candidates. The alternative is to exploit the existing method of Whiteley & Tholen (1998) and track the camera at the likeliest motion rate of the objects. In 2000, the time available is at best about an hour a night for the Venusian Lagrange points and about two hours for the Earth. In this time, the CCD frames need to be trimmed, biased, flat-fielded and searched for fast-moving objects, so that any discovery takes place in real-time.

The Venusian Lagrange points appear never to have been scanned before, although *The Global Astrometry Interferometer for Astrophysics* (GAIA) will perform this task when it flies in the next decade. Using the magnitude adjustments at the regions of greatest concentration on the sky, we estimate that GAIA will identify coorbiting Venusian asteroids with radii $\gtrsim 0.8$ km, as well as terrestrial asteroids with radii $\gtrsim 1$ km.

(2) For Mars, our sample is composed solely of tadpoles

alone. The greatest concentration of Trojans on the sky occurs at geocentric ecliptic latitudes of $\pm 9^\circ$ or, equivalently, heliocentric ecliptic latitudes of $\pm 12^\circ$, and does not occur in the ecliptic. The reason why the distribution is distended to quite high latitudes is that only inclined Martian Trojans are stable. The most likely velocity of the Trojans is $65'' \text{ hr}^{-1}$, significantly less than the Martian mean motion, while the FWHM of the velocity distribution is $32.3'' \text{ hr}^{-1}$. The two already known Martian Trojans (5261 Eureka and 1998 VF31) were discovered serendipitously by searches for Near Earth Objects. In fact, programs such as *The Lincoln Near Earth Asteroid Research Project* (LINEAR) provide the best existing constraints on the numbers of Martian Trojans. Assuming that LINEAR has surveyed the Martian L_5 point down to a completeness of $V \approx 17$, then we reckon that the number of undiscovered objects with radii greater than 0.1 km could still number several hundred. Within the next decade, GAIA will provide an all-sky inventory of solar system objects down to $V \approx 20$. It will be particularly valuable for objects out of the plane of the ecliptic. We estimate that Martian Trojans with typical radii of $\gtrsim 1.9$ km will be detectable by GAIA.

(3) For Mercury, our sample is composed solely of horseshoe orbits. True Trojans, or tadpole orbits, are not present as they do not survive on 100 Myr timescales. The most likely locations to find coorbiting satellites are at geocentric longitudes of $\ell_g \approx \pm 18^\circ$, or heliocentric longitudes of $\ell_h \approx 16.0^\circ$ and 348.5° . In other words, the most likely longitudes for discoveries are significantly displaced from the classical Lagrange points. These objects can have velocities exceeding $1000 \text{ arcsec hr}^{-1}$, although the most common velocity is $459 \text{ arcsec hr}^{-1}$, which is less than the Mercurian mean motion. Any ground-based searches for coorbiting Mercurian asteroids must take place during the day and concentrate on the L or possibly the K bands. The fields of view of infrared detectors are still quite small and so this is a daunting proposition. Nonetheless, Leake et al. (1987) covered two impressively large fields of view of 6 square degrees on either side of the Sun back in 1987. Leake et al.'s motivation was to look for Vulcanoids, and so their fields ($9^\circ \leq |\ell_g| \leq 12^\circ$) are not optimally located for our purposes. It would be interesting to repeat this experiment with fields sited around $\ell_g = \pm 18^\circ$. Another hopeful strategy is to use space-borne coronagraphs to search the area in the Solar System around the Sun for minor bodies.

ACKNOWLEDGMENTS

NWE is supported by the Royal Society, while ST acknowledges financial help from the European Community. We wish to thank John Chambers, Mark Lacy, Seppo Mikkola, Keith MacPherson, Prasenjit Saha and Scott Tremaine for helpful comments and suggestions. Tim de Zeeuw and Michael Perryman provided helpful information regarding GAIA, while Scott Tremaine and Robert Lupton helped us with SDSS. Above all, we are grateful to Jane Luu for much wise advise on strategies for observations and life.

REFERENCES

Bowell E., Hapke D., Domingue D., Lumme K., Peltoniemi J., Harris A. 1989, In "Asteroids II", eds. R. Binzel, T. Gehrels, M. Matthews, (Tucson, Univ. of Arizona Press), 524

Courten H., 1976, BAAS, 8, 504

Campins H., Davis D.R., Weidenschilling S.J., Magee M. 1996, In "Completing the Inventory of the Solar System", eds T.W. Rettig, J.M. Hahn, p. 85, (ASP Conf. Proc., Astron. Soc. Pacif., San Francisco)

Dunbar R.S., Helin E.F. 1983, BAAS, 15, 830

Evans N.W., Tabachnik S.A., 1999, Nature, 399, 41

Holt H.E., Levy D. 1990, IAU Circular No. 5045

Jewitt D., Luu J.X. 1999, In "Protostars and Planets IV", (Tucson, Univ. of Arizona Press), in press.

Kowal C.T. 1989, Icarus, 77, 118

Leake M.A., Chapman C.R., Weidenschilling S.J., Davis D.R., Greenberg R. 1987, Icarus, 68, 239

Lang K.R., 1980, Astrophysical Formulae, (Springer-Verlag, Berlin)

Luu J.X., Jewitt D. 1998, ApJ, 502, L91

Mikkola S., Innanen K.A., Muinonen K., Bowell E. 1994, Cel. Mech., 58, 53

Namouni F., Christou A.A., Murray C.D., 1999, Phys. Rev. Lett., 83, 2506

Tabachnik S.A., 1999, D. Phil. thesis, Oxford University (see "<http://www-thphys.physics.ox.ac.uk/users/Galactic/science/dphil.html>")

Tabachnik S.A., Evans N.W. 1999, ApJ, 517, L63

Tabachnik S.A., Evans N.W. 2000, MNRAS, submitted (Paper I)

Tombaugh C., In "Planets and Satellites", ed. G.P. Kuiper, B.M. Middlehurst, (University of Chicago Press, Chicago), 12

Weidenschilling S.J. 1978 Icarus, 35, 98

Weissman P.R., Wetherill G.W., 1974, AJ, 79, 404

Wiegert P.A., Innanen K., Mikkola S., 1997, Nature, 387, 685

Wiegert P.A., Innanen K., Mikkola S., 2000, Icarus, 145, 33

Wisdom J., 1980, AJ, 85, 1122

Whiteley R.J., Tholen D.J. 1998, Icarus, 136, 154

Zellner B., 1979, In "Asteroids", ed. T. Gehrels, (Tucson, Univ. of Arizona Press), 783